Water Resources Research

RESEARCH ARTICLE
10.1029/2020WR027290

# Factors Determining the Natural Fresh-Salt Groundwater Distribution in Deltas

**Joeri van Engelen**[1,2], **Marc F. P. Bierkens**[1,2], **Joost R. Delsman**[2], and **Gualbert H. P. Oude Essink**[1,2]

[1]Department of Physical Geography, Utrecht University, Utrecht, The Netherlands, [2]Unit of Subsurface and Groundwater Systems, Deltares, Utrecht, The Netherlands

**Key Points:**

- Global sensitivity analysis of a three-dimensional, variable-density groundwater model with complex paleo-hydrological boundary conditions
- The wide range of geometries, hydrogeological parameterizations, and boundary conditions is representative for many deltas worldwide
- Results suggest that fresh-salt groundwater distributions are not in dynamic equilibrium in at least half of the real-world cases analyzed

**Supporting Information:**

- Supporting Information S1
- Figure S1
- Figure S2
- Figure S3
- Figure S4

**Correspondence to:**
J. van Engelen,
joeri.vanengelen@deltares.nl

**Citation:**
van Engelen, J., Bierkens, M. F. P., Delsman, J. R., & Oude Essink, G. H. P. (2021). Factors determining the natural fresh-salt groundwater distribution in deltas. *Water Resources Research*, *57*, e2020WR027290. https://doi.org/10.1029/2020WR027290

Received 7 FEB 2020
Accepted 10 DEC 2020



**Abstract** Most river deltas are densely populated areas with intensive agriculture. The increased shortage of fresh surface water that results from rising demands are expected to lead to increased groundwater pumping, which leads to sea water intrusion. To correctly project the future of fresh groundwater resources in deltas, knowing the current fresh-salt groundwater distribution is a prerequisite. However, uncertainties about these distributions and their drivers are large. To understand these uncertainties, we conducted a global sensitivity analysis of a complex three-dimensional variable-density groundwater model of a synthetic delta, simulating the effect of the last glacial low stand and the subsequent marine transgression. The analysis is unique in its wide range of geometries, hydrogeological parameterizations, and boundary conditions analyzed, making it representative for a large number of deltas worldwide. We find that the aquifer hydraulic conductivity is the most uncertain input and has a strong nonmonotonous effect on the total salt mass onshore. The calculated fresh-salt groundwater distributions were classified into five classes and compared to real-world case studies. We find that salinity inversions occur in deltaic systems with high representative system anisotropies as a remnant of a marine transgression. These salinity inversions were observed in half of the real-world cases, indicating that their fresh-salt groundwater distributions are not in a dynamic equilibrium. We conclude that it is very likely that past marine transgressions are still reflected in the current fresh-salt groundwater distributions in deltas. This makes paleo-groundwater modeling a prerequisite for effective simulation of present-day groundwater salinity distributions in these systems.

**Plain Language Summary** Most river deltas are densely populated areas with intensive agriculture. The increased shortage of fresh surface water that results from rising demands are expected to lead to increased groundwater pumping, which, in turn, will lead to a more salinized groundwater system. To correctly project the future of fresh groundwater resources in deltas, knowing the current fresh-salt groundwater distribution is a prerequisite. However, uncertainties about the current fresh-salt groundwater distributions and their drivers are large. To understand these uncertainties, we conducted a lot of simulations of a complex three-dimensional groundwater model of a synthetic delta, simulating the effect of events that occurred tens of thousands of years ago. We compared these to fresh-salt groundwater distributions in the literature and find that it is very likely that these ancient events are still reflected in the current fresh-salt groundwater distributions in deltas.

## 1. Introduction

River deltas are of high socio-economic value, since they are often densely populated areas with high agricultural productivity (Neumann et al., 2015; Seto, 2011). The combination of growing population, increasingly intensive agriculture, and, in some areas, increased likelihood of droughts is expected to lead to fresh water shortages in surface water systems (Bucx et al., 2010). These stresses in turn will instigate more groundwater pumping, which leads to sea water intrusion and the upconing of saline groundwater (Michael et al., 2017; Werner et al., 2013). Despite that salinization poses a big problem to many large deltas (Rahman et al., 2019), the volume of fresh groundwater resources in many deltas is unknown, especially in the deeper parts of the groundwater system. While advances have been made in monitoring, especially with the onset of large-scale airborne electromagnetic (AEM) studies (King et al., 2018), 3D variable-density groundwater modeling still remains the only method to estimate a complete 3D fresh-salt groundwater distribution for large-scale groundwater systems (Faneca Sànchez et al., 2012). These models also have the added benefit

of studying the effects of past and future stresses on groundwater systems (Meyer et al., 2019; Oude Essink et al., 2010). Model results, however, are often uncertain due to the joint effects of uncertainty about the, often heterogeneous, hydraulic conductivity (Enemark et al., 2019), scarce validation data (Sanford & Pope, 2010), and uncertainty about past transient boundary conditions (van Engelen et al., 2018). The first two of these problems are common in hydrogeology (Domenico & Schwartz, 1990), but the latter problem deserves extra explanation. The fact that large-scale groundwater systems often have long residence times is well known (Jasechko et al., 2017; Sturchio et al., 2004). This also means that solute transport in these systems is influenced by paleo-boundary conditions (Kooi et al., 2000; Meisler et al., 1984), which can lead to at first glance surprising observations. For instance, brackish and saline groundwater zones that occur far inland in multiple deltas are correlated to past marine transgressions (Larsen et al., 2017). Likewise, offshore fresh groundwater, which is observed globally, is linked to glacial low stands (Post et al., 2013). Though constraining these paleo-boundary conditions is possible with the help of paleogeographical maps, seawater curves, and paleo-salinities (Delsman et al., 2014; Meyer et al., 2019; van Engelen et al., 2019), this information is rarely available over the whole time span of the model. This hampers the use of models to explain the origin of saline groundwater (van Engelen et al., 2018), which can be highly variable (Stuyfzand & Stuurman, 2006). Next to the previously mentioned contemporary sea water intrusion and marine transgressions, saline intrusion in rivers (Ayers et al., 2016; Faye et al., 2005), seepage of deep brines (Griffioen et al., 2016; Hanor, 1994), and evapoconcentration (Fass et al., 2007; Geirnaert & Laeven, 1992; Han et al., 2011) can increase groundwater salinity. Up to now, insights into the drivers of the current fresh-salt groundwater distribution in the world's deltas are fragmented and incomplete, as it is based on a limited number of modeled case studies and hydrogeochemical measurement campaigns; a systematic investigation is still lacking.

Sensitivity analyses are crucial to systematically investigate the effects of inputs and their influence on output uncertainty, thereby enhancing system understanding (Saltelli et al., 2004). We use “inputs” as an encompassing term for both model parameters (e.g., hydraulic conductivity) and boundary conditions (e.g., location shoreline), following the sensitivity analysis literature (Saltelli et al., 2004). There are plenty of studies that conducted a sensitivity analysis to investigate the effects of individual inputs on the fresh-salt groundwater distribution. A thorough overview of these studies is presented by Werner et al. (2013), to which we add a few examples not mentioned in that paper. These examples are all with 2D models, unless specified differently. Abarca et al. (2007) studied the effect of an aquifer slope parallel to the coast on the steady-state fresh-salt groundwater distribution with a 3D groundwater model, and found that this geometry can create quasi-horizontal circulation cells, to which the salt water wedge was more sensitive than the aquifer thickness or mechanical dispersion. Walther et al. (2017) investigated the effect of the slope of the sea-side boundary and found that this slope reduced the penetration length of the steady-state salt water wedge. In addition, this input had an increasing effect with increasing dispersivity and fresh water inflow, thus also showing input interaction. Ketabchi et al. (2016) used an inventive and exhaustive multimodel literature comparison to show that models with a fixed head boundary inland (head-controlled system) experienced more sea water intrusion due to sea level rise than those with a fixed flux inland (flux-controlled system). Moreover, they showed that the fresh-salt groundwater distribution is very sensitive to land surface inundation with sea water, especially in thick aquifers. Zamrsky et al. (2018) showed that the structure of the geology had a larger influence on the fresh-salt groundwater distribution than aquifer thickness. Rathore et al. (2018) found that in confined, stratified aquifers, under a constant transmissivity, the elevation of aquitards had a stronger influence on the shape of the salt water wedge than the ratio of the aquifer and aquitard hydraulic conductivity. Though these focused studies are very insightful, often the conducted sensitivity analyses are local, that is, inputs are varied one-at-a-time around one location in the input hyperspace. This in contrast to global sensitivity analyses, which aim to explore input sensitivity across the complete input hyperspace. Local sensitivity analyses may provide a distorted view of input sensitivities as they completely miss inputs that interact or have nonlinear effects on model output (Saltelli & Annoni, 2010). For example, Ebeling et al. (2019) conducted a global sensitivity analysis on a model that simulated the effect of hydraulic barriers to remediate sea water intrusion in an unconfined aquifer and concluded that the sensitivity of one input depended on the configuration of other inputs. Similar conclusions were drawn by Xu et al. (2018) for a variable-density groundwater model of a coastal karstic aquifer.

The above literature review showed that in order to fully understand which factors determine the onshore and offshore fresh-salt groundwater distributions in deltas, a sufficiently complex groundwater model is needed that is forced with paleo-boundary conditions and subject to a global sensitivity analysis. In this study, we use a variable-density groundwater flow model to conduct a global sensitivity analysis of the fresh-salt groundwater distribution on a synthetic delta aquifer with a realistic heterogenous but deterministic geology and complex paleo-boundary conditions. The analysis is unique in its wide range of geometries, hydrogeological parameterizations, and boundary conditions analyzed, making it representative for a large number of deltas worldwide. We focus on the natural fresh-salt groundwater distribution, since the development of the current fresh-salt groundwater distribution over long time scales is understudied, whereas plenty of research has been conducted on anthropogenic influence (Werner et al., 2013).

The remaining part of the paper is setup as follows. Section 2 describes the parameterization of the synthetic, fan-shaped delta aquifer, in particular its geometry and hydrogeology, as well as the initial and boundary conditions used in the density-dependent paleo-groundwater model. These inputs are based on a number of real-world case studies of existing deltas. The sensitivity analysis setup is described next, as well as how results are analyzed. Section 3 provides the results of the sensitivity analysis and compares the fresh-salt groundwater distributions with the real-world cases studied. These results and limitations to our study are further discussed in Section 4 followed by conclusions in Section 5.

## 2. Materials and Methods

We conducted a global sensitivity analysis on a model of 45 ka of variable-density groundwater flow in a synthetic, fan-shaped delta. A literature review was conducted to provide appropriate concepts and input ranges for the geometry, lithology, hydrogeology, and boundary conditions of the model (Section 2.6). Consequently, the effect of each input on the fresh-salt distribution was analyzed based on four metrics (Section 2.7). Furthermore, we classified the fresh-salt distributions into different types, linked these to inputs and compared these to fresh-salt distributions found in the literature.

### 2.1. Parameterizing Geometry

The geometry of the synthetic delta aquifer was created by first specifying a geometry in polar coordinates $(r, \varphi)$ (Figures 1a and 1c) and transforming this to a cartesian coordinate system $(x, y)$ (Figure 1b), creating a fan-shaped delta (Figure 1d). The reference depth was set to the present-day median eustatic sea level. The length of the model domain $L$ was fixed at 200 km, a representative size for major deltas; deltas with similar sizes are the Red River Delta (Vietnam), Chao Praya (Thailand), Rhine-Meuse (Netherlands), Nile (Egypt), and the Saloum (Senegal). $l_a$ specifies the relative length of the onshore part. The inputs $\alpha$, $\beta$, and $\gamma$, respectively, specified the slope of the onshore part, the coastal shelf, and coastal slope. Finally, $H_a$ and $H_b$, respectively, specified the depth of the aquifer at the apex and coast.

The hydrogeological base was created as a half-ellipsoid across the $\varphi z$-plane (Figure 1c), increasing in depth toward the coast (Figure 1a). For additional information, see supporting information S1. This half-ellipsoid shape is observed in, for example, the Yangtze Delta (Shi et al., 2012), the Pearl Delta (Zong et al., 2012), and the Red River Delta (Winkel et al., 2011). This geometry was consequently horizontally discretized into cells of $1 \times 1$ km (cf. van Engelen et al., 2018; Van Pham et al., 2019). Since $H_b$ varied widely, we did not fix the vertical discretization, but instead discretized the vertical into 100 cells to keep the load balance for each simulation roughly similar. This resulted in a vertical resolution ranging from 1 to 20 m (cf. van Engelen et al., 2018).

### 2.2. Hydrogeology

The lithology was created in a deterministic manner, where we specified a Holocene confining layer and a set of $N_{aqt}$ aquitards (Figures 1e, 1g, and 1h). The relative thickness of these layers was set with $f_{aqt}$, which is fraction of the sediment column that is aquitard (supporting information S1). The aquitards were created

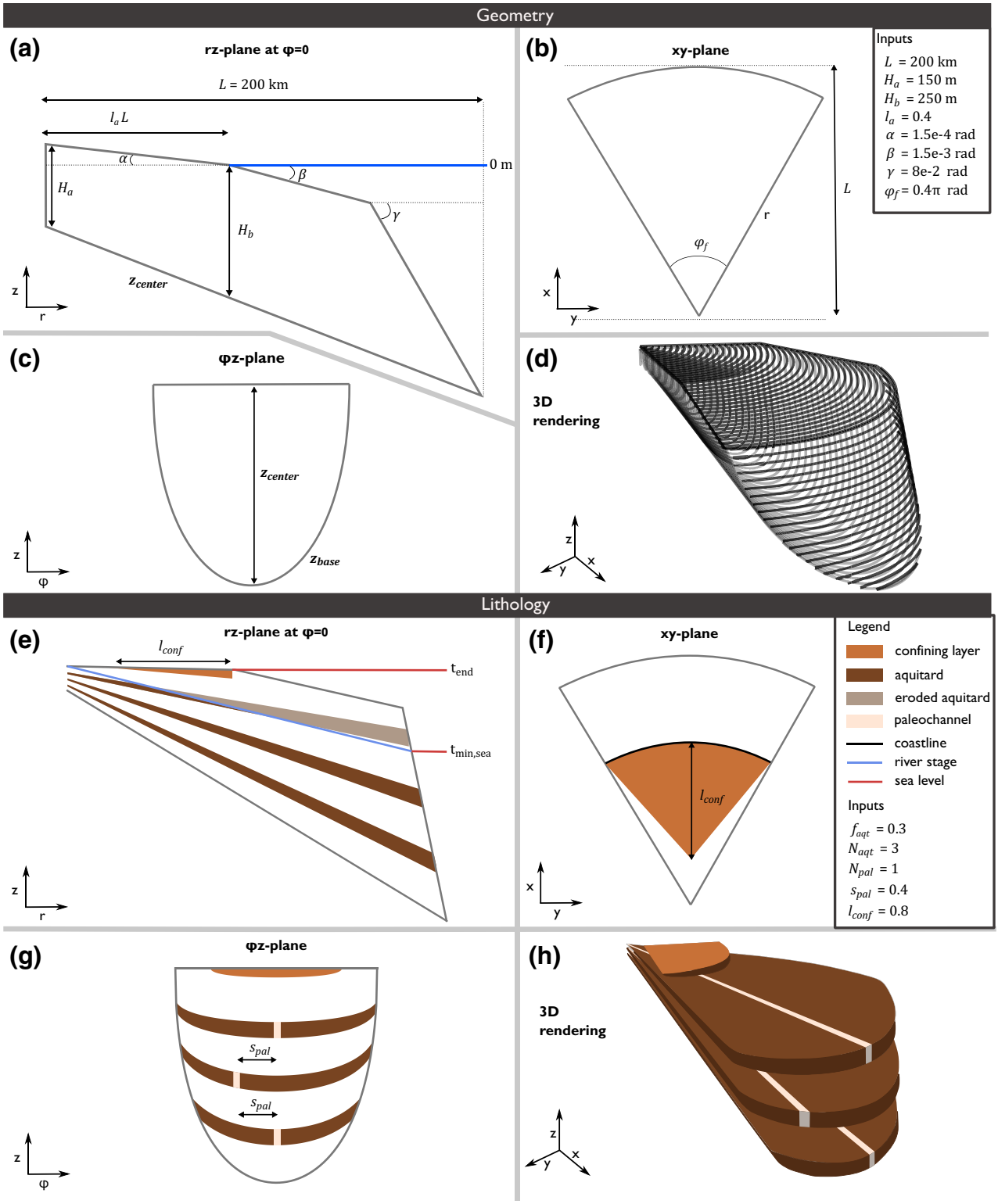


**Figure 1.** Visualization of the delta geometry and lithology across three planes. $r\phi$ and $xy$, respectively, are the polar and cartesian coordinate systems. (a) The $rz$-plane, on the left-hand side is the delta apex, and on the right-hand side the coast. The blue line indicates the reference depth. (b) The $xy$-plane, at the bottom is the delta apex, and at the top is the sea. (c) The $\phi z$-plane, note the half-ellipse-shaped bottom. (d) A rendering of the resulting geometry. The black lines visualize the top of the geometry, the gray lines the hydrogeological base. (e) Lithology across the $rz$-plane. The aquitard is eroded where it is intersected by the river stage during the glacial lowstand (at $t_{min,sea}$) (f) Lithology across the $xy$-plane, viewing the top confining layer. (g) Lithology across the $\phi z$-plane, note the paleochannels that form conducts through the aquitards. (h) 3D rendering of the aquitards and confining layer.

laterally continuous up to the apex, whereas the Holocene confining layer was not. This allowed for onshore recharge zones near the delta edges, similar to the infiltration zones near the edges of the Nile Delta (Pennington et al., 2017) and the Chao Praya delta (Sanford & Buapeng, 1996). The extent of the confining layer was set by $l_{\text{conf}}$ (Figure 1f), which specified how far up to the apex the layer reached.

A horizontal hydraulic conductivity was assigned to the aquifers ($K_{h,\text{aqf}}$) and a vertical hydraulic conductivity to the aquitards and confining layer ($K_{v,\text{aqt}}$). These were subsequently converted to, respectively, a $K_{v,\text{aqf}}$ and a $K_{h,\text{aqt}}$ with a formation anisotropy ( $K_h$ / $K_v$ ). This approach was chosen to unite the input distributions (Section 2.6) with the values found in the literature study (Figure 3). In the literature only a $K_{h,\text{aqf}}$ and a $K_{v,\text{aqt}}$ were usually provided, adhering to the main flow directions (Domenico & Schwartz, 1990).

Paleochannels were added as straight lines of 1-km width, a comparable width to paleochannels found in the Rhine-Meuse delta (van Asselen et al., 2017) and the West Bengal delta (Samadder et al., 2011). In the field, these channels can form either high conductive zones when filled up with fluvial sediments (Mulligan et al., 2007) or low conductive zones when filled up with marine sediments (Larsen et al., 2017). In this study, we focus on the paleochannels' ability to incise through aquitards and as such forming preferential flow paths with $f_{K,\text{pal}}$, which is a factor that governs the hydraulic conductivity of the paleochannels. The closer $f_{K,\text{pal}}$ is to 1, the more the hydraulic conductivity of the paleochannel tends to that of the aquifers. The horizontal distance between two vertically consecutive preferential flow paths can affect vertical flow (Post & Simmons, 2010) and is therefore incorporated as $s_{\text{pal}}$.

To increase the physical plausibility of the generated lithology, erosion was modeled by removing all aquitards that were located above any of the surface water profiles occurring from the last glacial low stand until present (Figure 2c). Furthermore, the confining layer is deposited after the Holocene transgression has reached its maximum extent ($t_{\text{tra}}$), which is comparable to how this confining layer was deposited in most deltas (Fielding et al., 2006; Pennington et al., 2017; Stanley & Warne, 1994; Tanabe et al., 2006).

## 2.3. Boundary Conditions

### 2.3.1. Offshore

The sea was incorporated as a Robin boundary condition (Jazayeri & Werner, 2019), which calculates the mass flux across the boundary ($Q_{\text{bnd}}$) as follows (Guo & Langevin, 2002):

$$Q_{\text{bnd}} = \rho_{\text{up}}\text{Cond}\left(h_{f,\text{bnd}} - h_{f,\text{cell}}\right) \tag{1}$$

where $\rho_{\text{up}}$ is the density upstream of the flow, so the density of the model cell with outward flow and the density of the sea with inward flow; Cond is the conductance of the boundary; and $h_{f,\text{bnd}}$ and $h_{f,\text{cell}}$ are the fresh water heads (Guo & Langevin, 2002; Langevin et al., 2003; Post et al., 2007) of, respectively, the boundary and model cell. We used the median eustatic sea level curve of the last 45 ka (Spratt & Lisiecki, 2016) to set the heads at the sea boundary. To simulate variable-density groundwater flow and coupled salt transport, we use iMOD-SEAWAT (see Section 2.5). This code requires heads to be constant throughout stress periods, thus we calculated the mean sea level over each stress period. Stress periods were refined during the Holocene (the last 11 ka, see Figure 2a), since this is the main period of interest where the marine transgression occurred. We use a coarser temporal discretization for the late Pleistocene as otherwise the amount of input data would get too large. The conductance between sea and aquifers and the salinity of the sea were kept constant through time at 1e5 $m^2$/d. This is on the high side compared to groundwater models that simulate the present-day Netherlands (De Lange et al., 2014), where values of 1e4 $m^2$/d are more common. However, we found that lower conductances (1e4 $m^2$/d) hampered free-convection during the marine transgression in simulations with lower $K_{h,\text{aqf}}$ values, despite Rayleigh number exceeding critical values (>40). The higher conductance is a reasonable assumption, since fine-grained sediments, which lower the conductance, started to be deposited relatively recently, during delta progradation (Stanley & Warne, 1994).

Sea cells were placed at the top active cells beyond the coastline. We use the point where sea level equals the topography, $r_{\text{sea=top}}$, to determine the location of the coastline during the late Pleistocene. This method, however, does not result in a marine transgression during the Holocene as the median sea level never

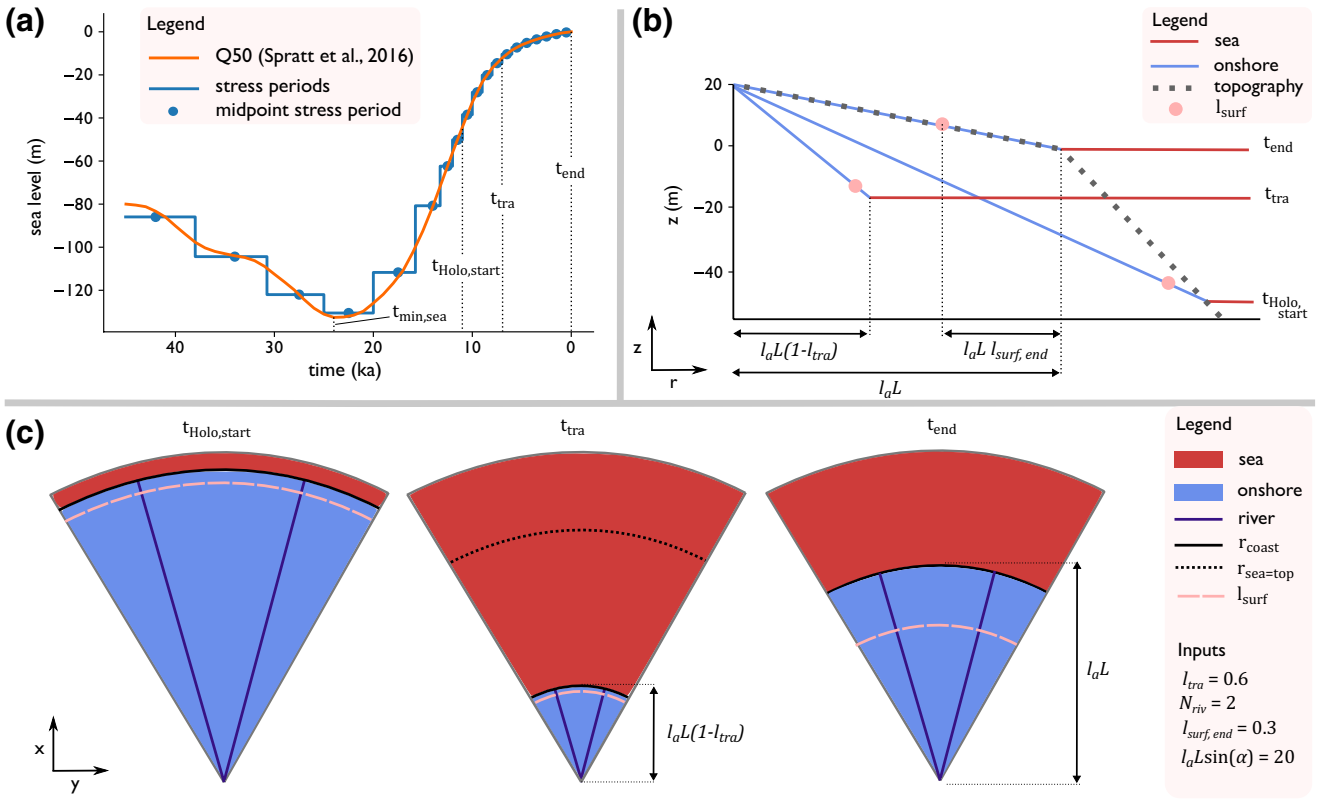


**Figure 2.** Description of the boundary conditions. (a) Eustatic sea level curve. In orange the median data of Spratt and Lisiecki (2016), in blue how we discretized this curve into constant stress periods. The vertical dotted lines indicate the sea levels at the glacial lowstand ($t_{min,sea}$), at the start of the Holocene ($t_{Holo,start}$), at the maximum extent of the marine transgression ($t_{tra}$), and at 0 ka ($t_{end}$). (b) Location of the boundary conditions over the *zr*-plane. On the right-hand side, the time each line belongs to. Note that the boundary conditions do not necessarily follow the (present-day) topography, because rivers can incise during lowstands and deltas prograded only after $t_{tra}$, which caused the present-day topography. (c) Location of the onshore and the offshore through time over the *xy*-plane.

reaches sea levels above 0 m. In reality, a lot of deltas experienced a marine transgression at the start of the Holocene, after which the delta progradation started as sea level rise decelerated (Stanley & Warne, 1994). To incorporate this without having to change the delta geometry, we therefore introduced $l_{tra}$ (supporting information S1), which is the relative length of the onshore part at $t_{end}$ (t = 0 ka) that is covered with sea water at the moment of maximum marine transgression $t_{tra}$. $t_{tra}$ varied in reality between 8,500 and 6,500 ka (Stanley & Warne, 1994).

### 2.3.2. Onshore

Onshore surface waters were also incorporated as a Robin boundary condition (Equation 1). Stages were assigned by drawing linear profiles from the delta apex to the contemporary coastline, following van Engelen et al. (2019). This boundary condition was assigned to all onshore cells with depths closest to the onshore surface water stage, so that a fan of, lower conductive, surface water was created. Hereafter, a number of $N_{riv}$ lines were drawn, each representing a large river branch. The conductance of onshore surface waters on these lines was multiplied with a factor, $f_{chan}$, to simulate the higher surface-groundwater interaction that occurs near large river branches (Sefelnasr & Sherif, 2014). The conductance was kept constant through time. Saline water intrusion in surface waters was incorporated by introducing a surface water saline intrusion length, $l_{surf}$, that specifies the extent of saline water intrusion at $t_{end}$ (Figure 2b). A linear salinity profile was drawn from $r_{coast}$ to $l_{surf}$, as a first-order approximation of the more S-shaped or exponential salinity profiles (Figure S1) observed in reality (Savenije, 2012). The intrusion length was corrected each stress period for

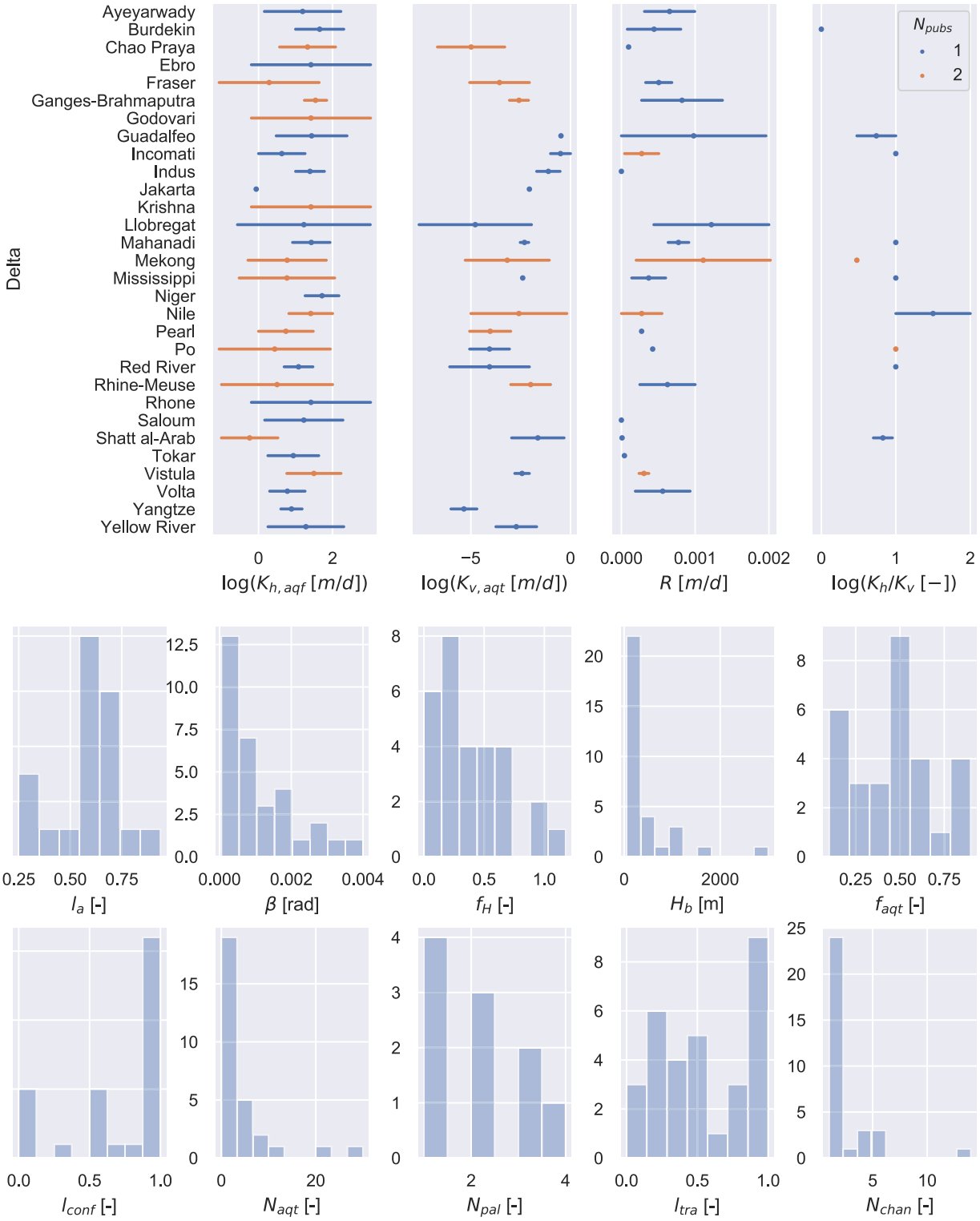


**Figure 3.** Distribution of inputs as found in the literature (previous compilations and additional real-world case studies, see Section 2.6). Inputs for which the input ranges are reported are plotted on top. Histograms at the bottom present the distribution of inputs for which no range was reported per delta.

the large changes in river gradient that occurred over time (supporting information S2), by substituting the Chezy formula (Chow et al., 1988) into Savenije's formula for the salinity intrusion length (Savenije, 2012).

A natural groundwater recharge flux ($R$) was assigned as a Neumann boundary condition at the upper active cells onshore, of which the magnitude was fixed throughout time. In reality, the natural groundwater recharge was very dynamic over the last 45 k years, as soil properties and climate varied strongly through this period (Gossel et al., 2010). The constant recharge was a first-order approximation of the model sensitivity to natural groundwater recharge. Adding more complex recharge functions would introduce more inputs, which would increase the amount of simulations required for the global sensitivity analysis (Section 2.5).

### 2.4. Initial Conditions

As initial salinity, we set all groundwater below the minimum sea level (−130 m) as saline. In this way, we accounted for older saline groundwater that might be present in deeper aquifers (Hanor, 1994; van Engelen et al., 2018). We traced this old saline groundwater with a separate tracer. The initial heads were set equal to the heads of the surface water systems during the first stress period, corrected for salinity such that the freshwater heads (Post et al., 2007) were vertically constant.

### 2.5. Sensitivity Analysis

In total, our global sensitivity analysis covered 23 inputs. Since the wall clock time of individual simulations ranged up to 7 days on a computational node with 24 cores a sampling scheme was chosen that sufficiently explored the input hyperspace while keeping the required amount of simulations to a minimum. One of the few methods capable of this is Morris' method (Morris, 1991), which therefore is a commonly used sampling scheme in hydrology (e.g., Cloke et al., 2008; Herman et al., 2013; Song et al., 2015; Xu et al., 2018). Morris' method works as follows. First, all input distributions are transformed to a uniform unit distribution, ranging from 0 to 1. Next, the resulting unit hyperspace is discretized into $N_{lev}$ levels. In this study, we set $N_{lev}$ to 4, which is a common value (Morris, 1991). Consequently, from a random starting point in this discretized hyperspace, one input at a time is varied consecutively. This results in a trajectory of length $N_{inp}+1$, where $N_{inp}$ is the number of inputs. An $N_{traj}$ number of trajectories is created so that the effect of changing one input at a time is evaluated multiple times for each input. In other words, the effect of each input can be assessed in different areas of the input hyperspace. The trick is to create a set of trajectories that covers the input hyperspace the best, for which multiple algorithms have been developed (Campolongo et al., 2007; Khare et al., 2015; Ruano et al., 2012). In this research, we use the algorithm of Khare et al. (2015) to create $N_{traj} = 10$ trajectories. The effect of each input is expressed as the elementary effect, which is the gradient of the change in model response (Section 2.7) over the change in input (Section 2.6). Since for each input $N_{traj}$ elementary effects are calculated, a mean ($\mu$) and standard deviation ($\sigma$) of the elementary effects can be calculated. The value $\mu$ serves as an estimate of the general sensitivity of the model to an input, $\sigma$ as a proxy for the amount of nonlinearity and/or interaction the input has. The higher the value of $\sigma$, the less likely a local sensitivity analysis is going to lead to an accurate assessment of the sensitivity of this input. Following Campolongo et al. (2007), we use the mean of the absolute elementary effects ($\mu^*$) to correct for nonmonotonous effects that otherwise cancel each other out. This also allows us to calculate a measure of nonmonotonicity, $\epsilon$, for each input:

$$\epsilon = \frac{\mathrm{abs}(\mu)}{\mu^*} \tag{2}$$

An $\epsilon$ close to one means the elementary effect of the input is very monotonous, meaning the sign of the model response to a change in the input is always equal, regardless of the configuration of other inputs. Conversely, an $\epsilon$ close to zero means it is very nonmonotonous.

**Table 1**
*List of the Chosen Input Distributions for the Global Sensitivity Analysis*

| Symbol | Description | Distribution | Range | Unit | Source |
|---|---|---|---|---|---|
| Geometry | | | | | |
| $l_a$ | Length of the onshore relative to the total length | Uniform | 0.1–0.8 | — | GEBCO (2014) |
| $f_H$ | Ratio sediment thickness at the apex over that at the coastline ($H_a$ / $H_b$) | Uniform | 0.0–0.8 | — | Data review |
| $H_b$ | Sediment thickness at the coastline | Loguniform | 70–1,000 | — | Data review |
| $A$ | Angle onshore topography | Loguniform | 1e-5–1e-3 | rad | Syvitski and Saito, (2007) |
| $B$ | Angle coastal shelf | Loguniform | 1e-4–4e-3 | rad | GEBCO (2014) |
| $\varphi_f$ | Angle sector across the *xy*-plane | Uniform | 0.125π–0.5π | rad | Assumed |
| Lithology | | | | | |
| $f_{aqt}$ | Fraction aquitard of the sediment column | Uniform | 0.1–0.8 | — | Data review |
| $l_{conf}$ | Extent of the confining layer relative to the total onshore length | Uniform | 0.0–1.0 | — | Data review |
| $N_{aqt}$ | Number of aquitards | Uniform | 0–6 | — | Data review |
| $N_{pal}$ | Number of paleochannels per aquitard | Uniform | 1–4 | — | Data review |
| $s_{pal}$ | Relative paleochannel displacement | Uniform | 0–1 | — | Data review |
| Hydrogeology | | | | | |
| $K_{h,aqf}$ | Horizontal hydraulic conductivity aquifer | Loguniform | 1e-1–2e2 | m/d | Data review |
| $K_{v,aqt}$ | Horizontal hydraulic conductivity aquitard | Loguniform | 1e-6–1e-1 | m/d | Data review |
| $f_{K,pal}$ | Factor governing horizontal hydraulic conductivity paleochannel | Uniform | 0–1 | — | Assumed |
| $K_h$ / $K_v$ | Anisotropy of single formation, assumed equal for aquifers and aquitards | Loguniform | 1–100 | — | Data review |
| $R$ | Recharge | Uniform | 0–3e-3 | m/d | Data review |
| Surface water | | | | | |
| $N_{chan}$ | Number of river channels | Uniform | 1–7 | — | Data review |
| $f_{chan}$ | Factor with which river channel resistance is reduced compared to surrounding surface water | Loguniform | 1–10 | — | Assumed |
| $l_{surf,end}$ | Salt water intrusion length in surface water at $t = 0$ ka relative to the onshore length | Uniform | 0–1 | — | Savenije (2012) |
| $l_{tra}$ | Length of maximum transgression relative to the onshore length | Uniform | 0–1 | — | Data review |
| $t_{tra}$ | Time of maximum trangression | Uniform | 9–6 | ka | Stanley and Warne (1994) |
| Solute transport | | | | | |
| $N$ | Effective porosity, assumed constant throughout domain | Uniform | 0.1–0.4 | — | Data review |
| $a_l$ | Longitudinal dispersivity | Loguniform | 0.25–10 | m | Zech et al. (2015) |

### 2.6. Input Distributions

A literature study was conducted to determine realistic input ranges. Table 1 lists the input distributions that were reported and varied in the sensitivity analysis. The inputs that were kept constant can be found in Table S1. For four inputs, complete overviews were already available from which a realistic input range could be inferred directly, namely the hydraulic gradient ($\alpha$) (Syvitski & Saito, 2007), the contemporary salinity intrusion length ($l_{surf,end}$) (Savenije, 2012), longitudinal dispersivity ($a_l$) (Zech et al., 2015), and time of maximum transgression ($t_{tra}$) (Stanley & Warne, 1994). For the other inputs, mainly those dealing with the subsurface, we compiled a database of real-world case studies for different deltas (Figure 3). The lithological inputs ($f_{aqt}$, $l_{conf}$, $N_{aqt}$, $N_{pal}$) and groundwater system depths ($H_a$,$H_b$) were determined from reported geological cross-sections; $l_{tra}$ and $N_{chan}$ from paleogeographical maps; and the remaining geometrical inputs ($l_a$, $\beta$) by drawing profiles through the General Bathymetric Chart of the Oceans (GEBCO, 2014). The literature sources usually provided a separate range of hydrogeological inputs $\left(K_{h,aqf}, K_{v,aqt}, K_h / K_v, R\right)$ in each delta.

The reported range either represented spatial variability of the input (zoning), variable lithology, different model scenarios, or had an unspecified cause. Two studies did not report $K_{v,\mathrm{aqt}}$, but instead very high effective anisotropies (~10,000) (Bonsor et al., 2017; Cao et al., 2016) for the entire groundwater system. In these cases, we used those anisotropies to calculate $K_{v,\mathrm{aqt}}$. The data of our literature review are included in the code package that accompanies this paper (van Engelen, 2020a).

### 2.7. Sensitivity Metrics

We computed sensitivity metrics to four outputs of interest, which we all evaluated at 0 ka. We work with relative volumes and masses as otherwise the sensitivity to geometrical inputs would dominate. First,

$$FW_{\mathrm{off}} = \frac{V_{f,\mathrm{off}}}{V_{\mathrm{off}}} \tag{3}$$

where $FW_{\mathrm{off}}$ is the relative volume of brackish (<10 g TDS/l cf. Post et al., 2013) groundwater offshore (–), $V_{f,\mathrm{off}}$ is the absolute volume of brackish groundwater offshore ($m^3$), and $V_{\mathrm{off}}$ are total volume of offshore groundwater ($m^3$). Second,

$$S_{\mathrm{on}} = \frac{M_{s,\mathrm{on}}}{M_{w,\mathrm{on}}} \tag{4}$$

$$S'_{\mathrm{on}} = \frac{\partial S_{\mathrm{on}}}{\partial t} \tag{5}$$

where $S_{\mathrm{on}}$ is the relative onshore salt mass (–), $M_{s,\mathrm{on}}$ is the absolute onshore salt mass (kg), and $M_{w,\mathrm{on}}$ is the absolute onshore water mass (kg), and $S'_{\mathrm{on}}$ is the time derivative of $S_{\mathrm{on}}$. Third,

$$S_{\mathrm{init}} = \frac{M_{s,\mathrm{init}}}{M_s} \tag{6}$$

where $S_{\mathrm{init}}$ is the relative mass of initial salt (–), $M_{s,\mathrm{init}}$ is the absolute mass of initial salt (kg), and $M_s$ is the absolute total salt mass (kg).

In addition, we visually classified the end-state (0 ka) fresh-salt groundwater distributions of each simulation into five different typologies, modified after the salinity distributions of the "modes of transgression" in Kooi et al. (2000): (1) the dispersive type, which has wide mixing zones (mode 1 in Kooi et al., 2000), (2) the free-convective type, where fingers are visible (modes 2 and 4 in Kooi et al., 2000), (3) a mix of the previous two types, (4) the advective type, with a narrow brackish zone spanning roughly three model cells, equaling 3 km, or less, and (5) the inverted type (mode 3 in Kooi et al., 2000), where salt water is overlaying fresher water. We consequently compared these to published fresh-salt groundwater distributions of real-world case studies that we classified in the same way.

### 2.8. Code Description and Computational Resources

We used iMOD-SEAWAT (Verkaik et al., 2017) to solve the combined variable-density groundwater flow and solute transport equations. This code is based on SEAWAT (Langevin et al., 2008), but supports distributed memory parallelization for a significant reduction in computation times. The SEAWAT code is the industry standard for solving variable-density groundwater and coupled salt transport problems. Therefore, the reader is referred to its manuals for an extensive explanation (Guo & Langevin, 2002; Langevin et al., 2003, 2008). All scripts to build, run, and postprocess models are released as a Python package (van Engelen, 2020a), which heavily utilized the iMOD-Python library (Visser & Bootsma, 2019). The global sensitivity analysis required 240 simulations. These were conducted on the Dutch national computational cluster Cartesius (Surfsara, 2014) on computational nodes with Intel Xeon E5-2690 v3 processors, each node hosting 24 CPU cores. The wall clock time of individual simulations varied strongly, ranging from 3 h to 7 days.

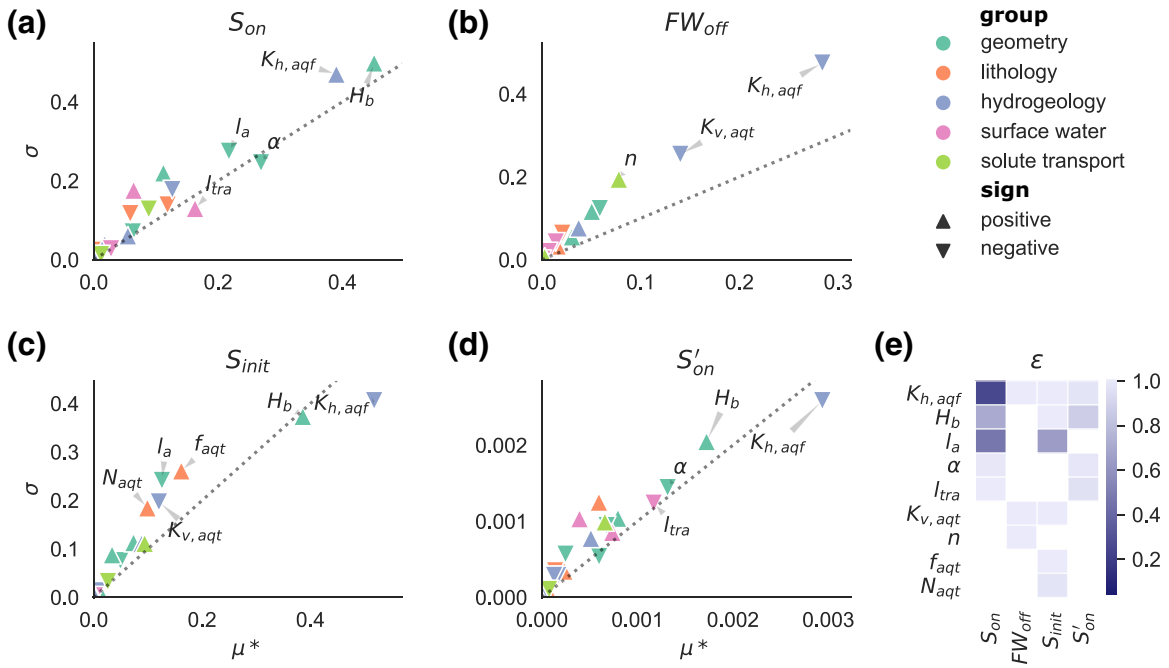


**Figure 4.** (a–d) Scatter plots of the mean absolute elementary effect ($\mu^*$) against its standard deviation ($\sigma$) of each input for the four metrics ($S_{on}$,$FW_{off}$, $S_{init}$, $S'_{on}$). Each input is represented by a triangle, the orientation of which indicates whether the input has a positive effect on the metric or not. The colors indicate the group the inputs belong to in Table 1. The dotted line represents where $\mu^* = \sigma$; inputs located above this line have a strong nonlinear effect or are strongly interacting. The labeled inputs are the most sensitive. (e) The monotonicity heatmap ($\varepsilon$) for all the labeled inputs per output: the closer this value is to 1, the more monotonous the response of a metric to a change in an input.

## 3. Results

The main results of the global sensitivity study are given in Figure 4, which shows that the onshore salinity mass $S_{on}$ is strongly controlled by the hydraulic conductivity of the aquifers $K_{h,aqf}$ (Figure 4a). This is a very nonmonotonous input for this variable (Figure 4e), meaning that an increase in $K_{h,aqf}$ can both increase and decrease the amount of salt water onshore, depending on the other inputs. More specifically, a high $K_{h,aqf}$ both favors vertical intrusion of saltwater during the marine transgression (converted via the anisotropy) as well as subsequently flushing infiltrated salt during a marine regression and flushing of initial salt over the complete time domain (Figure S2). Another, equally sensitive input is $H_b$, that largely determines the system thickness. A deeper system allows for relatively more salt onshore, since the salt water wedge can reach further inland as well as that the freshwater zone is relatively smaller with depth in a deep system in comparison to a shallow system. Furthermore, deeper systems have a higher capacity of preserving old salt. Next to these two dominant inputs, $S_{on}$ is controlled to a lesser degree by the relative onshore length ($l_a$), the hydraulic gradient ($\alpha$), and the extent of the marine transgression ($l_{tra}$). $l_a$ might be a surprising input to see here, since we normalize over the total onshore mass to calculate $S_{on}$. However, the brackish zone stays equal in size with a larger $l_a$ and hence decreases in relative size with increasing $l_a$. The fact that $S_{on}$ is more sensitive to $H_b$ than $l_{tra}$, implies that the amount of salt onshore $S_{on}$ is controlled more strongly by the amount of initial salt retained than the amount of salt infiltrated during the Holocene transgression.

The offshore brackish water ($FW_{off}$) is dominantly controlled by three inputs: $K_{h,aqf}$, the vertical conductivity of the aquitards $K_{v,aqt}$, and porosity $n$. $FW_{off}$ in our models was mainly the result of Pleistocene fresh water being preserved in the aquifers, instead of submarine groundwater discharge, which is the reason why this metric is mainly controlled by inputs that largely determine the velocity of the flow. Higher velocities result in a quicker replacement of fresh water with salt water.

Looking at the system dynamics, both $S'_{on}$ and the relative mass of initial salt $S_{init}$ are predominantly controlled by $K_{h,aqf}$ and $H_b$. The remaining sensitive inputs are different though, the short-term change in

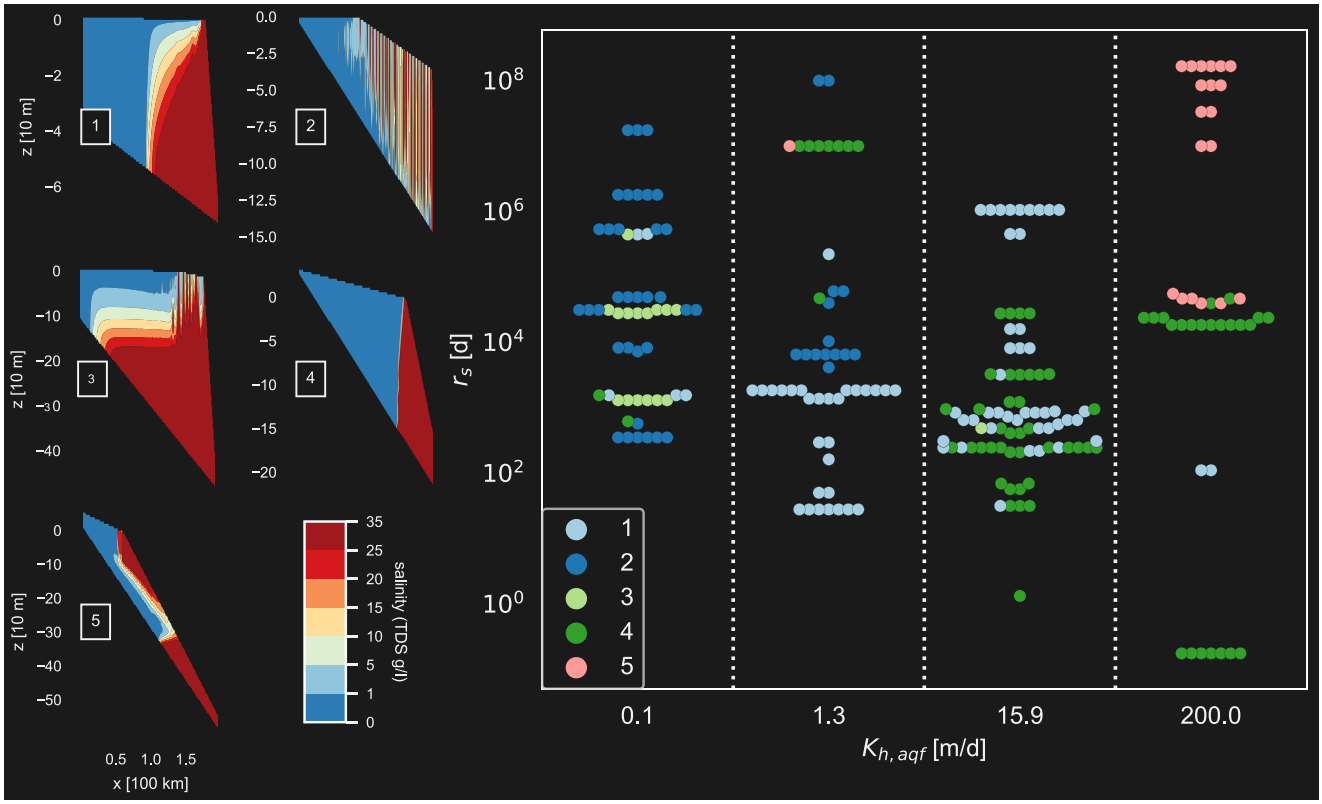


**Figure 5.** Left-hand side: Example 2D cross-sections of the groundwater salinity distributions of five simulations that are classified in the five different fresh-saline types (Section 2.7). The colors indicate the salinity. Right-hand side: Swarmplot of the fresh-saline types. The numbers in the legend point to a fresh-saline type (Section 2.7). On the *x*-axis the logarithm of the horizontal aquifer hydraulic conductivity, on the *y*-axis the resistance up to and including the first aquitard $r_s$ (Equation 7). Note that the *x*-axis is categorical, since we discretized the input hyperspace.

onshore salt mass $S'_{on}$ is additionally controlled by the hydraulic gradient $\alpha$ and extent of the marine transgression $l_{\text{tra}}$, whereas $S_{\text{init}}$ is additionally controlled by inputs that control the total clay resistance ($N_{\text{aqt}}$, $K_{v,\text{aqt}}$, $f_{\text{aqt}}$) and $l_a$. This means that, though $S_{\text{on}}$ is controlled strongly by the amount of initial salt retained by resistant layers, the current freshening or salinizing is controlled more strongly by the hydraulic gradient and the extent of the marine transgression.

The swarmplot in Figure 5 plots $K_{h,\text{aqf}}$ against the vertical resistance of the top sediments up to and including the first aquitard at the coastline ($r_s$ [d]). To calculate this, we summed the resistance of one aquifer and one aquitard, disregarding the resistance of the confining layer because this is deposited only after the Holocene transgression

$$r_s = H_b \left( \frac{f_{\text{aqt}}}{N_{\text{aqt}} K_{v,\text{aqt}}} + \frac{\left(1 - f_{\text{aqt}}\right) K_h \,/\, K_v}{\left(N_{\text{aqt}} + 1\right) K_{h,\text{aqf}}} \right) \tag{7}$$

Despite noise due to different boundary conditions for different simulations, patterns are visible. At lower hydraulic conductivities the system has a high probability of still being in a chaotic free-convective state. In some of these cases, the initial saline water in the aquifer was still preserved as a wide brackish zone, leading to the mixed type. With increasing $K_{h,\text{aqf}}$, a transition is visible toward an increased probability of the advective type. At high $K_{h,\text{aqf}}$ and $r_s$, meaning very high anisotropies of large-scale representative conductivities $K_{h,\,\text{rep}} \,/\, K_{v,\,\text{rep}}$, salinity inversions can occur.

Table 2 presents the results of a literature study where we classified all reported salinity distributions we could find for various deltas (a subset of the real-world case studies given in Figure 3). Only types 1 (with

**Table 2**
*Classification of Reported Fresh-Salt Water Distributions for Various Deltas Across the World*

| Delta | Country | Type | $K_{h,aqf}$ [m/d] | $r_s$ [d] | Source salt onshore | Reference |
|---|---|---|---|---|---|---|
| Ganges-Brahmaputra | Bangladesh and India | 5 | 20–70 | 5e4–4e5 | (Paleo)-salinity intrusion in rivers and aquaculture and marine transgression | Naus et al. (2019) and Sarker et al. (2018) |
| Incomati | Mozambique | 1 | 1–18 | 5e1—5e3 | Marine transgression | Nogueira et al. (2019) |
| Kelehantan | Malaysia | 5 | NaN | NaN | Marine transgression | Samsudin et al. (2008) |
| Llobregat | Spain | 1 | 1–1,000 | 4e3–1e9 | Holocene transgression (in aquitards) and Contemporary sea water intrusion (deep aquifer) | Iribar et al. (1997) and Manzano et al. (2001) |
| Mahanadi (South) | India | 1 | 8–85 | 7e3–2e4 | Unknown | Radhakrishna (2001) |
| Mahanadi (North) | India | 5 | 8–85 | 7e3–2e4 | Unknown | Radhakrishna (2001) |
| Mekong | Vietnam | 5 | 1–67.5 | 3e2–5e6 | Holocene transgression | Van Pham et al. (2019) |
| Nile | Egypt | 1 | 7–100 | 2e2–1e7 | Holocene transgression and evapoconcentration and rock salt dissolution | Geirnaert and Laeven (1992) and van Engelen et al. (2019) |
| Red River | Vietnam | 5 | 5–30 | 5e3–5e7 | Holocene transgression | Larsen et al. (2017) |
| Rhine-Meuse | The Netherlands | 1 | 0.1–100 | 1e2–9e3 | Holocene transgression and contemporary sea water intrusion | Delsman et al. (2014) |
| Rhone | France | 1 | NaN | NaN | Holocene transgression | de Montety et al. (2008) |
| Saloum | Senegal | 1 | 1–190 | 6e1–1e6 | Salinity intrusion in rivers | Faye et al. (2005) |
| Vistula | Poland | 1 | 9–168 | 7e3–4e4 | Pre-Holocene transgression | Kozerski (1983) |
| Yellow River | China | 5 | 2–200 | 6e2–7e4 | *Holocene transgression* | Cao et al. (2016) |

*Note*. Salt sources in cursive are hypothesized by us, in roman as hypothesized by the referenced authors. $K_{h,aqf}$ and $r_s$ are, respectively, retrieved and calculated from our data literature review.

wide mixing zones) and 5 (salinity inversion) are found in the reported field studies. If reported, we include the hypothesized source of the salt, and in one case we added a hypothesis ourselves. Namely, the Holocene transgression extended ~150 km landwards in the Yellow River Delta (Saito et al., 2001), which causes a similar salinity inversion in the neighboring southern coastal aquifers of the Laizhou Bay (Han et al., 2011). There are two cases of clear contemporary salt water intrusion. First, groundwater pumping in the ~70-m thick deeper aquifer of the Llobregat delta led to increased salinities (Iribar et al., 1997). In the Rhine-Meuse delta, peat excavation in the polders caused land surface levels below sea level, which consequently led to the polders draining (old marine) sea water (Delsman et al., 2014). In most cases, there were often relict salts of past transgressions present in the brackish and saline waters. Comparing the reported ranges of $K_{h,aqf}$ and values we estimated for $r_s$ for the respective deltas to the trend observed in Figure 5, we find that these comply with each other.

## 4. Discussion

The combination of a model with a large time domain and the global nature of our sensitivity analysis led to new insights. First, all the sensitivity metrics were very sensitive to hydraulic conductivity of the aquifers $K_{h,aqf}$ (Figure 4), which also had a very nonmonotonous effect on the onshore salt mass $S_{on}$, because $K_{h,aqf}$ both enhanced infiltration of salt water during the marine transgression as well as flushing of salt water from the system. This shows that care should be taken conducting a local sensitivity analysis on $K_{h,aqf}$ for transient models, as its effect on the total onshore salt mass at present depends on the configuration of other inputs. In sensitivity analyses with a more fixed geometry, the thickness of the groundwater system $H_b$ will be a more constrained input than $K_{h,aqf}$, which means that $K_{h,aqf}$ only increases in relative importance in these experiments.

In addition, from the abundance of type 5 salinity distributions (Figure 5), we conclude that a high $K_{h,\mathrm{aqf}}$ alone does not necessarily imply that the fresh-salt groundwater distribution is currently in a dynamic equilibrium. Moreover, as recently shown by van Engelen et al. (2019) (using a regional groundwater model with $K_{h,\mathrm{aqf}} = 75$ m/d), even groundwater salinity distributions with narrow brackish zones (type 4) can be still be affected by past conditions. In fact, the past occurrence of Holocene transgression in this case led to a steeper fresh-salt interface compared to the interface of an equivalent steady-state model.

Furthermore, we found that different time scales are influenced differently by inputs. We can infer this from a comparison between $S_{\mathrm{init}}$ and $S'_{\mathrm{on}}$. $S_{\mathrm{init}}$ is a measure of the long-term system dynamics (~40 ka), whereas $S'_{\mathrm{on}}$ is a measure of the shorter-term dynamics (~3 ka) (Figure 4): The long-term groundwater memory is predominantly controlled by clay resistance, whereas the shorter-term memory by the hydraulic gradient and the extent of the Holocene transgression. This has implications for groundwater dating studies in similar systems, as the long-term groundwater memory operates within the time scale of $^{14}$C groundwater dating (2–40 ka) and the shorter-term approaches the time scale of that of $^{39}$Ar (50 a–1,000 a) (Suckow, 2014).

Comparing the inferred typologies in Figure 5 to field cases provides a sense of the plausibility of the input configurations. Three of the five typologies are not observed in the real-world case-studies analyzed.

First, narrow brackish zones (type 4) are not observed, since all reviewed cases reported wide brackish zones. In the models narrow brackish zones, the transient boundary conditions and simple heterogeneities of our approach did not produce wide brackish zones. This means either that the reviewed deltas did not have a high effective aquifer conductivity $K_{h,\mathrm{aqf}}$, that the anisotropic cell dimensions numerically narrowed the brackish zone (Bakker & Hemker, 2002; Pauw et al., 2015), or that despite our best efforts, some important processes were not incorporated in this computational experiment. For instance, Michael et al. (2016) showed that stochastically generated hydraulic conductivity fields can create wide brackish zones, even with steady-state boundary conditions. Alternatively, kinetic mass transfer models, which are able to reproduce the tailing of a passing solute plume, also create wider brackish zones under transient conditions (Lu et al., 2009). We incorporated neither of these two approaches in our model setup, as constraining data was considered too scarce for this experiment. Generating stochastic hydraulic conductivity fields would require realistic parameters on spatial variation of conductivities or small-scale lithological variation for a wide range of deltas, which are not readily available. Also, the computational efforts needed to analyze the sensitivity to these parameters (a global sensitivity analysis, now with Monte Carlo sampling) would be at least an order of magnitude larger than the current study and is a topic for future research. Furthermore, estimates of the additional parameters required for kinematic mass transfer models are very limited (Sanford et al., 2017).

Second, free-convection (types 2 and 3) events are not observed in the field on a large scale, only as short-lived events on smaller scales (Andersen et al., 2007; Stevens et al., 2009; Van Dam et al., 2009). We are not aware of any reported large-scale, free-convective systems on a delta scale, which raises doubts on the realism of an aquifer with a representative conductivity $K_{v,\mathrm{aqf}}$ between 0.001 and 0.1 m/d. Instead, chaotic salinity patterns are now often ascribed to heterogeneity in lithology and salt sources (e.g., Delsman et al., 2014; Michael et al., 2016; Naus et al., 2019; van Engelen et al., 2019). Given that many deltas have experienced a Holocene transgression (Larsen et al., 2017), the lack of free-convection distribution in real-world cases provides an additional constraint on $K_{v,\mathrm{aqf}}$ and thus indirectly on $K_{h,\mathrm{aqf}}$. Because nearly all the simulations with $K_{h,\mathrm{aqf}} = 0.1$ m/d were classified as the free-convective type, we deem it unlikely that deltaic aquifers would have a representative hydraulic conductivity on a regional scale that approaches this value.

In contrast, the case-studies analyzed suggest that a high resistance up to and including the first aquitard $r_s$ and high $K_{h,\mathrm{aqf}}$, in other words a high representative anisotropy $\left(K_{h,\mathrm{rep}} \,/\, K_{v,\mathrm{rep}}\right)$, results in a high probability of retaining an overtopping (type 5). For instance, the Quaternary aquifer underlying the Yellow River Delta has a high representative anisotropy and shows a brackish zone overlying fresh water (Cao et al., 2016). Similarly, high values of $\left(K_{h,\mathrm{rep}} \,/\, K_{v,\mathrm{rep}}\right)$ were required to reproduce the observed salinity inversion in the Red River Delta (Larsen et al., 2017). The strongly heterogeneous Ganges-Brahmaputra delta also has a very high $K_{h,\mathrm{rep}} \,/\, K_{v,\mathrm{rep}}$ (Michael & Voss, 2009) and an observed salinity inversion at 200 m depth (Sarker et al., 2018).

Three salt sources were included our model: pre-Holocene salt water, Holocene sea water, and saline water by intrusion in rivers. The model results turned out to be very sensitive to the total amount of salt present initially, which we infer from the fact that $S_{on}$ was very sensitive to $H_b$. With increasing system thickness, there was an increasing amount of initial salt still present and longer travel times for sea water circulation. Despite that this old salt water can occupy large fractions of larger deltaic groundwater systems, its origins and flow paths are often underexplored in case studies and thus uncertain (Griffioen et al., 2016; Han et al., 2011; van Engelen et al., 2018). The fact that $S_{on}$ was more sensitive to the extent of the marine transgression $l_{tra}$ than the saline intrusion length in rivers $l_{surf,end}$ implies that the amount of salt water intruded via rivers was usually less in our modeled groundwater systems than the amount of Holocene sea water, despite that the Holocene transgression occurred only temporarily. This is a result of both the salinity and the hydraulic gradient of the river systems that stimulate flushing with fresher water, contrary to the constant sea level and salinity of the sea. The relatively small effect of salt water originating from rivers is also observed in case studies, as a local phenomenon constrained to areas in proximity to (paleo)-channels in the upper ~50 m of the groundwater system (Ayers et al., 2016; Faye et al., 2005; Naus et al., 2019).

Despite our best efforts, there are limitations to this study. Even though we conducted an exhaustive literature study to attain realistic input distributions, this could not prevent some unrealistic input combinations for two reasons. First, as mentioned earlier in the discussion, delta aquifers with a regional-scale representative hydraulic conductivity of 0.1 m/d presumably do not exist, as this would result in large-scale, free-convective systems that are still present, which are not observed in the field. This means that the range of our $K_{h,aqf}$ input distribution is too large, meaning that the sensitivity to this input may be overestimated. Second, we disregarded anthropogenic effects. One case where clear large-scale anthropogenic influence on the fresh-salt groundwater distribution is the heavily engineered Rhine-Meuse delta (Delsman et al., 2014), mainly because of the land reclamation projects that cause large upward head gradients from 1850 AD up to now. Table 2, however, shows that humans did not influence the large-scale fresh-salt groundwater distribution for most deltas (yet). If human influence is observed, it is in the shallow aquifers (e.g., Ganges-Brahmaputra). A rigorous study where the human impacts on the fresh-salt groundwater distribution are quantified in deltaic systems is a topic for further study. In addition, our classification is based on visual interpretation, introducing subjectivity. A possible solution to this problem is presented by Werner (2016), who created a classification of fresh-salt groundwater distributions based on analytical solutions. However, this framework is not (yet) suitable for classifying the complex outputs produced by our 3D models. Finally, we have not conducted this sensitivity analysis on a set of dimensionless equations. This would have made this analysis scale-independent and could have provided some additional insights on input interactions. The dimensionless equations derived by Abarca et al. (2007) for the anisotropic dispersive Henry problem can serve as a good starting point for this. However, these authors found that some of the key factors, that control the outputs of interest in their study, were not explicitly present in their dimensionless equations. This means that these equations alone are not enough to identify all key factors, meaning a rigorous analysis is still necessary. The simulations conducted in this study would not satisfy the criterion of evenly distributed input discretization across the dimensionless input hyperspace, required for a successful application of Morris method (Section 2.5). Suppose we would use the simulations of this research to study the dimensionless equations, we therefore cannot guarantee that these simulations identify key controlling dimensionless inputs. We additionally note that a full dimensionless analysis would have had only limitedly reduced the number of inputs analyzed according to the Buckingham-Pi theorem, that is, from 23 to 20, since we have three fundamental dimensions (Mass, Time, Length).

## 5. Conclusion

We conducted a unique global sensitivity analysis of a model with complex boundary conditions over geological time scales. The analysis is unique in its wide range of geometries, hydrogeological parameterizations, and boundary conditions analyzed, making it representative for a large number of deltas worldwide. Model results, in particular onshore saline and its gradient, proved to be highly sensitive to the aquifer hydraulic conductivity ($K_{h,aqf}$) and thickness of groundwater system ($H_b$), and to a lesser degree to the hydraulic gradient ($\alpha$) and the extent of the Holocene transgression ($l_{tra}$). We showed a nonmonotonous sensitivity to $K_{h,aqf}$ on the total salt mass onshore, indicating interactions between the various model inputs. Furthermore,

by classifying the model groundwater salinity distributions and comparing these with distributions of real-world cases, we showed that in at least half of these cases, the groundwater salinity distribution is not in a dynamic equilibrium. This is most likely caused by a combination of past marine transgressions and high effective anisotropies. We conclude that it is very likely that past marine transgressions are still reflected in the current fresh-salt groundwater distributions in deltas. This makes paleo-groundwater modeling a prerequisite for effective simulation of current groundwater salinity distributions in these systems.

## Data Availability Statement

3D renderings of all 240 model results can be found online under the following DOI (van Engelen, 2020b): https://doi.org/10.5281/zenodo.3653876. The code and data to reproduce the models and figures can be found under the following DOI (van Engelen, 2020a): https://doi.org/10.5281/zenodo.3653734.

**Acknowledgments**
We like to thank Perry de Louw for his helpful suggestions for our model setup. Furthermore, we like to thank two anonymous reviewers and Daniel Fernàndez-Garcia for helping to improve this manuscript. This research has been supported by the Nederlandse Organisatie voor Wetenschappelijk Onderzoek (NWO) under the New Delta program (grant 869.15.013). This work was carried out on the Dutch national e-infrastructure with the support of the SURF Cooperative, on a NWO Pilot Project Grant. The authors declare that they have no conssflict of interest.

## References

Abarca, E., Carrera, J., Sánchez-Vila, X., & Dentz, M. (2007). Anisotropic dispersive Henry problem. *Advances in Water Resources*, *30*(4), 913–926. https://doi.org/10.1016/j.advwatres.2006.08.005

Abarca, E., Carrera, J., Sánchez-Vila, X., & Voss, C. I. (2007). Quasi-horizontal circulation cells in 3D seawater intrusion. *Journal of Hydrology*, *339*(3–4), 118–129. https://doi.org/10.1016/j.jhydrol.2007.02.017

Andersen, M. S., Jakobsen, R., Nyvang, V., Christensen, F. D., Engesgaard, P., & Postma, D. (2007). Density-driven seawater plumes in a shallow aquifer caused by a flooding event—Field observations, consequences for geochemical reactions and potentials for remediation schemes. In *GQ07: Securing groundwater Quality in Urban and Industrial Environments, Proceedings of the 6th international groundwater quality conference held in fremantle* (pp. 2–7), Western Australia.

Ayers, J. C., Goodbred, S., George, G., Fry, D., Benneyworth, L., Hornberger, G., et al. (2016). Sources of salinity and arsenic in groundwater in southwest Bangladesh. *Geochemical Transactions*, *17*(1), 4. https://doi.org/10.1186/s12932-016-0036-6

Bakker, M., & Hemker, K. (2002). A Dupuit formulation for flow in layered, anisotropic aquifers. *Advances in Water Resources*, *25*(7), 747–754. https://doi.org/10.1016/S0309-1708(02)00074-X

Bonsor, H. C., MacDonald, A. M., Ahmed, K. M., Burgess, W. G., Basharat, M., Calow, R. C., et al. (2017). Hydrogeological typologies of the Indo-Gangetic basin alluvial aquifer, South Asia. *Hydrogeology Journal*, *25*(5), 1377–1406. https://doi.org/10.1007/s10040-017-1550-z

Bucx, T., Marchand, M., Makaske, B., & van de Guchte, C. (2010). *Comparative assessment of the vulnerability and resilience of 10 deltas—synthesis report* Delft-Wageningen. Retrieved from www.delta-alliance.org

Campolongo, F., Cariboni, J., & Saltelli, A. (2007). An effective screening design for sensitivity analysis of large models. *Environmental Modelling and Software*, *22*(10), 1509–1518. https://doi.org/10.1016/j.envsoft.2006.10.004

Cao, G., Han, D., Currell, M. J., & Zheng, C. (2016). Revised conceptualization of the North China Basin groundwater flow system: Groundwater age, heat and flow simulations. *Journal of Asian Earth Sciences*, *127*, 119–136. https://doi.org/10.1016/j.jseaes.2016.05.025

Chow, V. T., Maidment, D. R., & Mays, L. W. (1988). Applied hydrology. In B. J. Clark, & J. Morriss (Eds.), McGraw-Hill series in water resources and environmental engineering, Internatio. (Vol. 1, pp. 512). Singapore: McGraw-Hill Book Co.

Cloke, H. L., Pappenberger, F., & Renaud, J. P. (2008). Multi-Method Global Sensitivity Analysis (MMGSA) for modelling floodplain hydrological processes. *Hydrological Processes*, *22*, 1660–1674.

De Lange, W. J., Prinsen, G. F., Hoogewoud, J. C., Veldhuizen, A. A., Verkaik, J., Oude Essink, G. H. P., et al. (2014). An operational, multi-scale, multi-model system for consensus-based, integrated water management and policy analysis: The Netherlands Hydrological Instrument. *Environmental Modelling and Software*, *59*, 98–108. https://doi.org/10.1016/j.envsoft.2014.05.009

de Montety, V., Radakovitch, O., Vallet-Coulomb, C., Blavoux, B., Hermitte, D., & Valles, V. (2008). Origin of groundwater salinity and hydrogeochemical processes in a confined coastal aquifer: Case of the Rhône delta (Southern France). *Applied Geochemistry*, *23*(8), 2337–2349. https://doi.org/10.1016/j.apgeochem.2008.03.011

Delsman, J. R., Hu-A-Ng, K. R. M., Vos, P. C., De Louw, P. G. B., Oude Essink, G. H. P., Stuyfzand, P. J., & Bierkens, M. F. P. (2014). Paleo-modeling of coastal saltwater intrusion during the Holocene: An application to the Netherlands. *Hydrology and Earth System Sciences*, *18*(10), 3891–3905. https://doi.org/10.5194/hess-18-3891-2014

Domenico, P. A., & Schwartz, F. W. (1990). *Physical and chemical hydrogeology* (1st ed.). Toronto, ON: John Wiley & Sons.

Ebeling, P., Händel, F., & Walther, M. (2019). Potential of mixed hydraulic barriers to remediate seawater intrusion. *The Science of the Total Environment*, *693*, 133478. https://doi.org/10.1016/j.scitotenv.2019.07.284

Enemark, T., Peeters, L. J. M., Mallants, D., & Batelaan, O. (2019). Hydrogeological conceptual model building and testing: A review. *Journal of Hydrology*, *569*, 310–329. https://doi.org/10.1016/j.jhydrol.2018.12.007

Faneca Sànchez, M., Gunnink, J. L., van Baaren, E. S., Oude Essink, G. H. P., Siemon, B., Auken, E., et al. (2012). Modelling climate change effects on a Dutch coastal groundwater system using airborne electromagnetic measurements. *Hydrology and Earth System Sciences*, *16*(12), 4499–4516. https://doi.org/10.5194/hess-16-4499-2012

Fass, T., Cook, P. G., Stieglitz, T., & Herczeg, A. L. (2007). Development of saline ground water through transpiration of sea water. *Ground Water*, *45*(6), 703–710. https://doi.org/10.1111/j.1745-6584.2007.00344.x

Faye, S., Maloszewski, P., Stichler, W., Trimborn, P., Faye, S. C., & Gaye, C. B. (2005). Groundwater salinization in the Saloum (Senegal) delta aquifer: Minor elements and isotopic indicators. *Science of the Total Environment*, *343*(1–3), 243–259. https://doi.org/10.1016/j.scitotenv.2004.10.001

Fielding, C. R., Trueman, J. D., & Alexander, J. (2006). Holocene depositional history of the Burdekin River Delta of Northeastern Australia: A model for a low-accommodation, Highstand Delta. *Journal of Sedimentary Research*, *76*(3), 411–428. https://doi.org/10.2110/jsr.2006.032

GEBCO. (2014). *GEBCO dataset*. Retrieved from http://www.gebco.net/data_and_products/gridded_bathymetry_data/gebco_30_second_grid/

Geirnaert, W., & Laeven, M. P. (1992). Composition and history of ground water in the western Nile Delta. *Journal of Hydrology*, *138*(1–2), 169–189. https://doi.org/10.1016/0022-1694(92)90163-P

Gossel, W., Sefelnasr, A., & Wycisk, P. (2010). Modelling of paleo-saltwater intrusion in the northern part of the Nubian Aquifer System, Northeast Africa. *Hydrogeology Journal*, *18*(6), 1447–1463. https://doi.org/10.1007/s10040-010-0597-x

Griffioen, J., Verweij, H., & Stuurman, R. (2016). The composition of groundwater in Palaeogene and older formations in the Netherlands. A synthesis. *Netherlands Journal of Geosciences*, *95*(3), 349–372. https://doi.org/10.1017/njg.2016.19

Guo, W., & Langevin, C. D. (2002). *User's guide to SEAWAT: A computer program for simulation of three-dimensional variable-density ground-water flow. USGS techniques of water resources investigations*. Tallahassee: United States Geological Survey.

Han, D., Kohfahl, C., Song, X., Xiao, G., & Yang, J. (2011). Geochemical and isotopic evidence for palaeo-seawater intrusion into the south coast aquifer of Laizhou Bay, China. *Applied Geochemistry*, *26*(5), 863–883. https://doi.org/10.1016/j.apgeochem.2011.02.007

Hanor, J. S. (1994). Origin of saline fluids in sedimentary basins. *Geological Society, London, Special Publications*, *78*(1), 151–174. https://doi.org/10.1144/GSL.SP.1994.078.01.13

Herman, J. D., Kollat, J. B., Reed, P. M., & Wagener, T. (2013). Technical note: Method of Morris effectively reduces the computational demands of global sensitivity analysis for distributed watershed models. *Hydrology and Earth System Sciences*, *17*(7), 2893–2903. https://doi.org/10.5194/hess-17-2893-2013

Iribar, V., Carrera, J., Custodio, E., & Medina, A. (1997). Inverse modelling of seawater intrusion in the Llobregat delta deep aquifer. *Journal of Hydrology*, *198*(1–4), 226–244. https://doi.org/10.1016/S0022-1694(96)03290-8

Jasechko, S., Perrone, D., Befus, K. M., Bayani Cardenas, M., Ferguson, G., Gleeson, T., et al. (2017). Global aquifers dominated by fossil groundwaters but wells vulnerable to modern contamination. *Nature Geoscience*, *10*, 425–430. https://doi.org/10.1038/ngeo2943

Jazayeri, A., & Werner, A. D. (2019). Boundary condition nomenclature confusion in groundwater flow modelling. *Groundwater*, *57*(5), 664–668. https://doi.org/10.1111/gwat.12893

Ketabchi, H., Mahmoodzadeh, D., Ataie-Ashtiani, B., & Simmons, C. T. (2016). Sea-level rise impacts on seawater intrusion in coastal aquifers: Review and integration. *Journal of Hydrology*, *535*, 235–255. https://doi.org/10.1016/j.jhydrol.2016.01.083

Khare, Y. P., Muñoz-Carpena, R., Rooney, R. W., & Martinez, C. J. (2015). A multi-criteria trajectory-based parameter sampling strategy for the screening method of elementary effects. *Environmental Modelling and Software*, *64*, 230–239. https://doi.org/10.1016/j.envsoft.2014.11.013

King, J., Oude Essink, G., Karaolis, M., Siemon, B., & Bierkens, M. F. P. (2018). Quantifying geophysical inversion uncertainty using airborne frequency domain electromagnetic data—Applied at the Province of Zeeland, the Netherlands. *Water Resources Research*, *54*, 8420–8441. https://doi.org/10.1029/2018WR023165

Kooi, H., Groen, J., & Leijnse, A. (2000). Modes of seawater intrusion during transgressions. *Water Resources Research*, *36*(12), 3581–3589. https://doi.org/10.1029/2000WR900243

Kozerski, B. (1983). Problems of the salt water origin in the Vistula Delta aquifers. In *Proceedings of the 8th salt water intrusion meeting* (pp. 325–334), Bari, Italy.

Langevin, C. D., Shoemaker, W. B., & Guo, W. (2003). *MODFLOW-2000, the U.S. Geological Survey modular ground-water model-documentation of the SEAWAT-2000 version with the variable-density flow process (VDF) and the integrated MT3DMS transport process (IMT)*. Retrieved from http://water.usgs.gov/ogw/seawat/

Langevin, C. D., Thorne, D. T. Jr., Dausman, A. M., Sukop, M. C., & Guo, W. (2008). SEAWAT version 4: A computer program for simulation of multi-species solute and heat transport. In D. Kempthorne, & M. D. Myers (Eds.), *U.S. Geological Survey techniques and methods book 6* (pp. 39). Reston, VA: United States Geological Survey.

Larsen, F., Tran, L. V., Van Hoang, H., Tran, L. T., Christiansen, A. V., & Pham, N. Q. (2017). Groundwater salinity influenced by Holocene seawater trapped in incised valleys in the Red River delta plain. *Nature Geoscience*, *10*, 376–382. https://doi.org/10.1038/ngeo2938

Lu, C., Kitanidis, P. K., & Luo, J. (2009). Effects of kinetic mass transfer and transient flow conditions on widening mixing zones in coastal aquifers. *Water Resources Research*, *45*, W12402. https://doi.org/10.1029/2008WR007643

Manzano, M., Custodio, E., Loosli, H., Cabrera, M. C., Riera, X., & Custodio, J. (2001). Palaeowater in coastal aquifers of Spain. *Geological Society, London, Special Publications*, *189*(1), 107–138. https://doi.org/10.1144/gsl.sp.2001.189.01.08

Meisler, H., Leahy, P. P., & Knobel, L. L. (1984). Effect of eustatic sea-level changes on saltwater-freshwater in the Northern Atlantic Coastal Plain. In W. P. Clark, & D. L. Peck (Eds.), *USGS water supply paper: 2255* (pp. 28). Alexandria, VA: United States Geological Survey.

Meyer, R., Engesgaard, P., & Sonnenborg, T. O. (2019). Origin and dynamics of saltwater intrusion in a regional aquifer: Combining 3-D saltwater modeling with geophysical and geochemical data. *Water Resources Research*, *55*, 1792–1813. https://doi.org/10.1029/2018WR023624

Michael, H. A., Post, V. E. A., Wilson, A. M., & Werner, A. D. (2017). Science, society, and the coastal groundwater squeeze. *Water Resources Research*, *53*, 2610–2617. https://doi.org/10.1002/2017WR020851

Michael, H. A., Scott, K. C., Koneshloo, M., Yu, X., Khan, M. R., & Li, K. (2016). Geologic influence on groundwater salinity drives large seawater circulation through the continental shelf. *Geophysical Research Letters*, *43*, 10782–10791. https://doi.org/10.1002/2016GL070863

Michael, H. A., & Voss, C. I. (2009). Estimation of regional-scale groundwater flow properties in the Bengal Basin of India and Bangladesh. *Hydrogeology Journal*, *17*(6), 1329–1346. https://doi.org/10.1007/s10040-009-0443-1

Morris, M. D. (1991). Factorial sampling plans for preliminary computational experiments. *Technometrics*, *33*(2), 161–174. https://doi.org/10.2307/1269043

Mulligan, A. E., Evans, R. L., & Lizarralde, D. (2007). The role of paleochannels in groundwater/seawater exchange. *Journal of Hydrology*, *335*(3–4), 313–329. https://doi.org/10.1016/j.jhydrol.2006.11.025

Naus, F. L., Schot, P., Groen, K., Matin Ahmed, K., & Griffioen, J. (2019). Groundwater salinity variation in Upazila Assasuni (southwestern Bangladesh), as steered by surface clay layer thickness, relative elevation and present-day land use. *Hydrology and Earth System Sciences*, *23*(3), 1431–1451. https://doi.org/10.5194/hess-23-1431-2019

Neumann, B., Vafeidis, A. T., Zimmermann, J., & Nicholls, R. J. (2015). Future coastal population growth and exposure to sea-level rise and coastal flooding—A global assessment. *PLoS ONE*, *10*(3), e0131375. https://doi.org/10.1371/journal.pone.0118571

Nogueira, G., Stigter, T. Y., Zhou, Y., Mussa, F., & Juizo, D. (2019). Understanding groundwater salinization mechanisms to secure freshwater resources in the water-scarce city of Maputo, Mozambique. *Science of the Total Environment*, *661*, 723–736. https://doi.org/10.1016/j.scitotenv.2018.12.343

Oude Essink, G. H. P., Van Baaren, E. S., & De Louw, P. G. B. (2010). Effects of climate change on coastal groundwater systems: A modeling study in the Netherlands. *Water Resources Research*, *46*, W00F04. https://doi.org/10.1029/2009WR008719

Pauw, P. S., Van der Zee, S. E. A. T. M., Leijnse, A., Delsman, J. R., De Louw, P. G. B., De Lange, W. J., & Oude Essink, G. H. P. (2015). Low-resolution modeling of dense drainage networks in confining layers. *Groundwater*, *53*(5), 771–781. https://doi.org/10.1111/gwat.12273

Pennington, B. T., Sturt, F., Wilson, P., Rowland, J., & Brown, A. G. (2017). The fluvial evolution of the Holocene Nile Delta. *Quaternary Science Reviews*, *170*, 212–231. https://doi.org/10.1016/j.quascirev.2017.06.017
Post, V. E. A., Groen, J., Kooi, H., Person, M., Ge, S., & Edmunds, M. W. (2013). Offshore fresh groundwater reserves as a global phenomenon. *Nature*, *504*(7478), 71–78. https://doi.org/10.1038/nature12858
Post, V. E. A., Kooi, H., & Simmons, C. T. (2007). Using hydraulic head measurements in variable-density ground water flow analyses. *Ground Water*, *45*(6), 664–671. https://doi.org/10.1111/j.1745-6584.2007.00339.x
Post, V. E. A., & Simmons, C. T. (2010). Free convective controls on sequestration of salts into low-permeability strata: Insights from sand tank laboratory experiments and numerical modelling. *Hydrogeology Journal*, *18*(1), 39–54. https://doi.org/10.1007/s10040-009-0521-4
Radhakrishna, I. (2001). Saline fresh water interface structure in Mahanadi delta region, Orissa, India. *Environmental Geology*, *40*, 369–380. https://doi.org/10.1007/s002540000182
Rahman, M. M., Penny, G., Mondal, M. S., Zaman, M. H., Kryston, A., Salehin, M., et al. (2019). Salinization in large river deltas: Drivers, impacts and socio-hydrological feedbacks. *Water Security*, *6*, 100024. https://doi.org/10.1016/j.wasec.2019.100024
Rathore, S. S., Zhao, Y., Lu, C., & Luo, J. (2018). Defining the effect of stratification in coastal aquifers using a new parameter. *Water Resources Research*, *54*, 5948–5957. https://doi.org/10.1029/2018WR023114
Ruano, M. V., Ribes, J., Seco, A., & Ferrer, J. (2012). An improved sampling strategy based on trajectory design for application of the Morris method to systems with many input factors. *Environmental Modelling and Software*, *37*, 103–109. https://doi.org/10.1016/j.envsoft.2012.03.008
Saito, Y., Yang, Z., & Hori, K. (2001). The Huanghe Yellow River and Changjiang Yangtze River deltas: A review on their characteristics, evolution and sediment discharge during the Holocene. *Geomorphology*, *41*, 219–231.
Saltelli, A., & Annoni, P. (2010). How to avoid a perfunctory sensitivity analysis. *Environmental Modelling and Software*, *25*(12), 1508–1517. https://doi.org/10.1016/j.envsoft.2010.04.012
Saltelli, A., Tarantola, S., Campolongo, F., & Ratto, M. (2004). In A. Saltelli (Ed.), *Sensitivity analysis in practice: A guide to assessing scientific models* (1st ed.). Chichester, England: John Wiley & Sons. https://doi.org/10.1002/0470870958
Samadder, R. K., Kumar, S., & Gupta, R. P. (2011). Paleochannels and their potential for artificial groundwater recharge in the western Ganga plains. *Journal of Hydrology*, *400*(1–2), 154–164. https://doi.org/10.1016/j.jhydrol.2011.01.039
Samsudin, A. R., Haryono, A., Hamzah, U., & Rafek, A. G. (2008). Salinity mapping of coastal groundwater aquifers using hydrogeochemical and geophysical methods: A case study from north Kelantan, Malaysia. *Environmental Geology*, *55*(8), 1737–1743. https://doi.org/10.1007/s00254-007-1124-9
Sanford, W. E., & Buapeng, S. (1996). Assessment of a groundwater flow model of the Bangkok Basin, Thailand. *Hydrogeology Journal*, *4*, 26–40. https://doi.org/10.1007/s100400050083
Sanford, W. E., Plummer, L. N., Casile, G., Busenberg, E., Nelms, D. L., & Schlosser, P. (2017). Using dual-domain advective-transport simulation to reconcile multiple-tracer ages and estimate dual-porosity transport parameters. *Water Resources Research*, *53*, 5002–5016. https://doi.org/10.1002/2016WR019469
Sanford, W. E., & Pope, J. P. (2010). Current challenges using models to forecast seawater intrusion: Lessons from the Eastern Shore of Virginia, USA. *Hydrogeology Journal*, *18*(1), 73–93. https://doi.org/10.1007/s10040-009-0513-4
Sarker, M. M. R., Van Camp, M., Islam, M., Ahmed, N., & Walraevens, K. (2018). Hydrochemistry in coastal aquifer of southwest Bangladesh: Origin of salinity. *Environmental Earth Sciences*, *77*(2), 39. https://doi.org/10.1007/s12665-017-7196-2
Savenije, H. H. G. (2012). *Salinity and tides in alluvial estuaries*.Retrieved from https://doi.org/10.1016/B978-044452107-1/50006-X
Sefelnasr, A., & Sherif, M. (2014). Impacts of seawater rise on seawater intrusion in the Nile Delta Aquifer, Egypt. *Groundwater*, *52*(2), 264–276. https://doi.org/10.1111/gwat.12058
Seto, K. C. (2011). Exploring the dynamics of migration to mega-delta cities in Asia and Africa: Contemporary drivers and future scenarios. *Global Environmental Change*, *21*(Suppl. 1), S94–S107. https://doi.org/10.1016/j.gloenvcha.2011.08.005
Shi, X., Fang, R., Wu, J., Xu, H., Sun, Y. Y., & Yu, J. (2012). Sustainable development and utilization of groundwater resources considering land subsidence in Suzhou, China. *Engineering Geology*, *124*(1), 77–89. https://doi.org/10.1016/j.enggeo.2011.10.005
Song, X., Zhang, J., Zhan, C., Xuan, Y., Ye, M., & Xu, C. (2015). Global sensitivity analysis in hydrological modeling: Review of concepts, methods, theoretical framework, and applications. *Journal of Hydrology*, *523*(225), 739–757. https://doi.org/10.1016/j.jhydrol.2015.02.013
Spratt, R. M., & Lisiecki, L. E. (2016). A Late Pleistocene sea level stack. *Climate of the Past*, *12*(4), 1079–1092. https://doi.org/10.5194/cp-12-1079-2016
Stanley, D. J., & Warne, A. G. (1994). Worldwide initiation of Holocene marine deltas by deceleration of sea-level rise. *Science*, *265*, 228–231. https://doi.org/10.1126/science.265.5169.228
Stevens, J. D., Sharp, J. M., Simmons, C. T., & Fenstemaker, T. R. (2009). Evidence of free convection in groundwater: Field-based measurements beneath wind-tidal flats. *Journal of Hydrology*, *375*(3–4), 394–409. https://doi.org/10.1016/j.jhydrol.2009.06.035
Sturchio, N. C., Du, X., Purtschert, R., Lehmann, B. E., Sultan, M., Patterson, L. J., et al. (2004). One million year old groundwater in the Sahara revealed by krypton-81 and chlorine-36. *Geophysical Research Letters*, *31*, L05503. https://doi.org/10.1029/2003GL019234
Stuyfzand, P. J., & Stuurman, R. J. (2006). Origin, distribution and chemical mass balances of non-anthropogenic, brackish and (hyper) saline groundwaters in the Netherlands. In G., Barrocu (Ed.), *Proceedings 1st SWIM-SWICA Joint Saltwater Intrusion Conference, Cagliari-Chia Laguna, Italy-September 24–29, 2006* (pp. 151–164). Cagliari: SWIM.
Suckow, A. (2014). The age of groundwater—Definitions, models and why we do not need this term. *Applied Geochemistry*, *50*, 222–230. https://doi.org/10.1016/j.apgeochem.2014.04.016
Surfsara. (2014). *Description of the Cartesius system*. Retrieved May 14, 2018, from https://userinfo.surfsara.nl/systems/cartesius/description
Syvitski, J. P. M., & Saito, Y. (2007). Morphodynamics of deltas under the influence of humans. *Global and Planetary Change*, *57*(3–4), 261–282. https://doi.org/10.1016/j.gloplacha.2006.12.001
Tanabe, S., Saito, Y., Lan Vu, Q., Hanebuth, T. J. J., Lan Ngo, Q., & Kitamura, A. (2006). Holocene evolution of the Song Hong (Red River) delta system, northern Vietnam. *Sedimentary Geology*, *187*(1–2), 29–61. https://doi.org/10.1016/j.sedgeo.2005.12.004
van Asselen, S., Cohen, K. M., & Stouthamer, E. (2017). The impact of avulsion on groundwater level and peat formation in delta floodbasins during the middle-Holocene transgression in the Rhine-Meuse delta, The Netherlands. *Holocene*, *27*(11), 1694–1706. https://doi.org/10.1177/0959683617702224
Van Dam, R. L., Simmons, C. T., Hyndman, D. W., & Wood, W. W. (2009). Natural free convection in porous media: First field documentation in groundwater. *Geophysical Research Letters*, *36*, L11403. https://doi.org/10.1029/2008GL036906
van Engelen, J. (2020). *delta_aquifer*. https://doi.org/10.5281/zenodo.3653734

van Engelen, J. (2020). *Video supplement: Factors determining the natural fresh-salt groundwater distribution in deltas (Version v1)*. Zenodo. Retrieved from http://doi.org/10.5281/zenodo.3653876

van Engelen, J., Oude Essink, G. H. P., Kooi, H., & Bierkens, M. F. P. (2018). On the origins of hypersaline groundwater in the Nile Delta aquifer. *Journal of Hydrology*, *560*, 301–317. https://doi.org/10.1016/j.jhydrol.2018.03.029

van Engelen, J., Verkaik, J., King, J., Nofal, E. R., Bierkens, M. F. P., & Oude Essink, G. H. P. (2019). A three-dimensional palaeohydrogeological reconstruction of the groundwater salinity distribution in the Nile Delta Aquifer. *Hydrology and Earth System Sciences*, *23*, 5175–5198. https://doi.org/10.5194/hess-2019-151

Van Pham, H., van Geer, F. C., Tran, V. B., Dubelaar, W., & Oude Essink, G. H. P. (2019). Paleo-hydrogeological reconstruction of the fresh-saline groundwater distribution in the Vietnamese Mekong Delta since the late Pleistocene. *Journal of Hydrology: Regional Studies*, *23*, 22.

Verkaik, J., Van Engelen, J., Huizer, S., & Oude Essink, G. H. P. (2017). The new parallel Krylov Solver for SEAWAT. *AGU Fall Meeting 2017*, New Orleans, Louisiana.

Visser, M., & Bootsma, H. (2019). *iMOD-Python: Work with iMOD MODFLOW models in Python*. Retrieved from https://imod.xyz/

Walther, M., Graf, T., Kolditz, O., Liedl, R., & Post, V. (2017). How significant is the slope of the sea-side boundary for modelling seawater intrusion in coastal aquifers? *Journal of Hydrology*, *551*, 648–659. https://doi.org/10.1016/j.jhydrol.2017.02.031

Werner, A. D. (2016). On the classification of seawater intrusion. *Journal of Hydrology*, *551*, 619–631. https://doi.org/10.1016/j.jhydrol.2016.12.012

Werner, A. D., Bakker, M., Post, V. E. A., Vandenbohede, A., Lu, C., Ataie-Ashtiani, B., et al. (2013). Seawater intrusion processes, investigation and management: Recent advances and future challenges. *Advances in Water Resources*, *51*, 3–26. https://doi.org/10.1016/j.advwatres.2012.03.004

Winkel, L. H. E., Pham, T. K. T., Vi, M. L., Stengel, C., Amini, M., Nguyen, T. H., et al. (2011). Arsenic pollution of groundwater in Vietnam exacerbated by deep aquifer exploitation for more than a century. *Proceedings of the National Academy of Sciences of the United States of America*, *108*(4), 1246–1251. https://doi.org/10.1073/pnas.1011915108

Xu, Z., Hu, B. X., & Ye, M. (2018). Numerical modeling and sensitivity analysis of seawater intrusion in a dual-permeability coastal karst aquifer with conduit networks. *Hydrology and Earth System Sciences*, *22*(1), 221–239. https://doi.org/10.5194/hess-22-221-2018

Zamrsky, D., Oude Essink, G. H. P., & Bierkens, M. F. P. (2018). Estimating the thickness of unconsolidated coastal aquifers along the global coastline. *Earth System Science Data*, *10*(3), 1591–1603. https://doi.org/10.5194/essd-10-1591-2018

Zech, A., Attinger, S., Cvetkovic, V., Dagan, G., Dietrich, P., Fiori, A., et al. (2015). Is unique scaling of aquifer macrodispersivity supported by field data? *Water Resources Research*, *51*, 7662–7679. https://doi.org/10.1002/2015WR017220

Zong, Y., Huang, K., Yu, F., Zheng, Z., Switzer, A., Huang, G., et al. (2012). The role of sea-level rise, monsoonal discharge and the palaeo-landscape in the early Holocene evolution of the Pearl River delta, southern China. *Quaternary Science Reviews*, *54*, 77–88. https://doi.org/10.1016/j.quascirev.2012.01.002